Article

Remote Sensing Monitoring and Analysis of Jinwuco Lateral Moraine Landslide-Glacial Lake Outburst in Southeast Tibet

Yaping Gao [1], Wenguang Yang [1,2], Rui Guo [2,3,*] and Liming Jiang [2,3]

1   College of Earth Science, Chengdu University of Technology, Chengdu 610059, China
2   State Key Laboratory of Geodesy and Earth's Dynamics, Innovation Academy for Precision Measurement Science and Technology, Chinese Academy of Sciences, Wuhan 430077, China
3   University of Chinese Academy of Sciences, Beijing 100049, China
*   Correspondence: guorui@apm.ac.cn

Abstract: On 25 June 2020, a glacial lake outburst flood (GLOF) occurred in Jinwuco, Nidou Zangbo, and southeast Tibet, causing catastrophic damage to multiple infrastructures such as roads, bridges, and farmlands in the surrounding and downstream areas. Due to the lack of long-term monitoring of glacial lake and glacier changes in the region and the surrounding surface, the spatial and temporal evolutionary characteristics and triggering factors of the disaster still need to be determined. Here, we combine multi-temporal optical remote sensing image interpretation, surface deformation monitoring with synthetic aperture radar (SAR)/InSAR, meteorological observation data, and corresponding soil moisture change information to systematically analyze the spatial and temporal evolution characteristics and triggering factors of this GLOF disaster. Optical images taken between 1987 and 2020 indicate that the glacial lake's initial area of 0.39 km^2 quickly grew to 0.56 km^2, then plummeted to 0.26 km^2 after the catastrophe. Meanwhile, we found obvious signs of slippage beside the lateral moraine at the junction of the glacier's terminus and the glacial lake. The pixel offset tracking (POT) results based on SAR images acquired before and after the disaster reveal that the western lateral moraine underwent a 40 m line of sight (LOS) deformation. The small baseline subset InSAR (SBAS-InSAR) results from 2017 to 2021 show that the cumulative deformation of the slope around the lateral moraine increased in the rainy season before the disaster, with a maximum cumulative deformation of −52 mm in 120 days and gradually stabilized after the disaster. However, there are three long-term deformation areas on the slope above it, showing an increasing trend after the disaster, with cumulative deformation exceeding −30 mm during the monitoring period. The lateral moraine collapse occurred in a warm climate with continuous and intense precipitation, and the low backscatter intensity prior to the slide suggests that the soil was very moist. Intense rainfall is thought to be the catalyst for lateral moraine collapse, whereas the lateral moraine falling into the glacier lake is the direct cause of the GLOF. This study shows that the joint active–passive remote sensing technique can accurately obtain the spatial and temporal evolution characteristics and triggering factors of GLOF. It is helpful to understand the GLOF event caused by the slide of lateral moraine more comprehensively, which is essential for further work related to glacial lake hazard assessment.

Keywords: GLOF; active-passive remote sensing; InSAR; spatio-temporal evolutionary characteristics

1. Introduction

Glaciers in alpine regions exhibit a general trend of retreat and thinning due to global warming [1–6]. The glacial lakes have expanded rapidly [7], which raises the likelihood of glacial lake outburst floods (GLOF) events [8,9]. Southeast Tibet has the most severe glacier loss on the Tibetan Plateau [10,11]. In recent years, the quantity and size of glacial lakes in the region have increased significantly, and several GLOF incidents have occurred, severely damaging local infrastructure and compromising the lives and property of residents [12–14]. Detailed analysis and discussion of GLOF events and an in-depth understanding of the

spatial and temporal evolution characteristics and triggers of GLOFs will help improve the ability to assess and manage GLOF risks, establish a scientific and practical early warning and forecasting system, and mitigate and avoid the impact of GLOFs [15,16]. Currently, the study of GLOFs in southeastern Tibet primarily focuses on identifying potentially dangerous glacial lakes in the region and assessing the risk of glacial lakes [17,18]. There needs to be more comprehensive research on the spatial and temporal evolution characteristics and triggering factors of glacial lake outburst disasters [19]. According to the 6th IPCC Special Report on Oceans and Cryosphere in a Changing Climate [20], glacier retreat can expose mountain slopes that were initially covered/supported by the glacier, which can significantly increase the potential for slope instability. The expanding glacial lake is surrounded by steep slopes and lateral moraines [21]. Recent GLOF studies have gradually begun to analyze and discuss the impact of lateral moraine collapse on disasters [22,23].

Since GLOFs often occur in mountainous areas with complex and remote topography, it is difficult to carry out relevant monitoring using traditional measurements. Thanks to the rapid development of remote sensing technology, it provides adequate data support and technical support for our study of GLOF [24]. Optical images are now widely used in GLOF and related glacier disasters [25,26]. However, due to the influence of cloudy and rainy weather in the summer, it is sometimes impossible to effectively obtain the feature information of the occlusion area, which seriously hinders its application scenarios and timeliness [27]. Considering the rich phase and magnitude information of SAR images and the advantages of all-day and all-weather observation, this can continuously and effectively observe the ground surface and make up for the shortage of optical remote sensing images [28,29]. Based on the phase information of SAR images, we can use InSAR technology to obtain the subtle long-time series deformation of the ground surface around the glacial lake, which helps to discern the stability of the regional ground surface and identify potential landslide areas. By capturing anomalous surface deformation signals before the disaster, it is possible to analyze GLOF triggers in conjunction with other factors (e.g., meteorological factors). When the surface deformation is too large, the pixel offset tracking technique based on SAR intensity information can be used as a complement InSAR technique to obtain large gradient surface deformation [30–34]. At the same time, radar backscattering intensity can reflect the moist state of soil [35,36], which helps analyze the change in surface water content before disaster strikes.

In this paper, we comprehensively analyze the Jinwuco GLOF in June 2020 using a combination of optical remote sensing and SAR/InSAR techniques. First, we used multi-temporal remote sensing data to obtain the results of glacier retreat and glacial lake area expansion for a long time series from 1987 to 2020 while identifying the lateral moraine slip and surface destruction areas after GLOF. The SAR-POT technique was then used to obtain the overall surface deformation around the glacial lake before and after the disaster. Subsequently, the SBAS-InSAR technique was used to monitor and analyze the long-time series of deformation of the surface around the glacial lake from 2017 to 2021. The displacement time series around the slip zone was selected to evaluate the main influencing factors of lateral moraine displacement. Finally, we discuss the triggers of this GLOF event and the potential risks of surface deformation and post-disaster existence around the glacial lake.

2. Study Area and Datasets

2.1. Study Area

The study area is located in the eastern part of Nyainqentanglha, Qinghai-Tibet Plateau, China, in the Nidou Zangbo ("Zangbo" refers to rivers in Tibetan) watershed, which is part of Jiali County, Naqu City, Tibet Autonomous Region (Figure 1). The valley is a sub-basin located in the upper reaches of the Yi'ong Zangbo, with a total length of 68 km. The topography in the basin is high in the west and low in the east; the highest elevation is 6883 m, the lowest elevation is 3110 m, and the average elevation is higher than 5000 m. The basin has a subcool semi-humid monsoon plateau climate with cool summers and

cold winters, and rainfall is mainly concentrated in summer, accounting for 60–70% of the year [12]. According to the observation records from 1980 to 2019 at the nearest Lhari weather stations in the study area, −0.2 °C in January is the average annual minimum temperature, 8.9 °C in July is the average annual maximum temperature, and the average annual cumulative rainfall is 753 mm [14]. The widely distributed marine glaciers in the basin, with a total area of 417.96 km². This glacier is more sensitive to climate change than continental glaciers in the Tibetan Plateau [37].
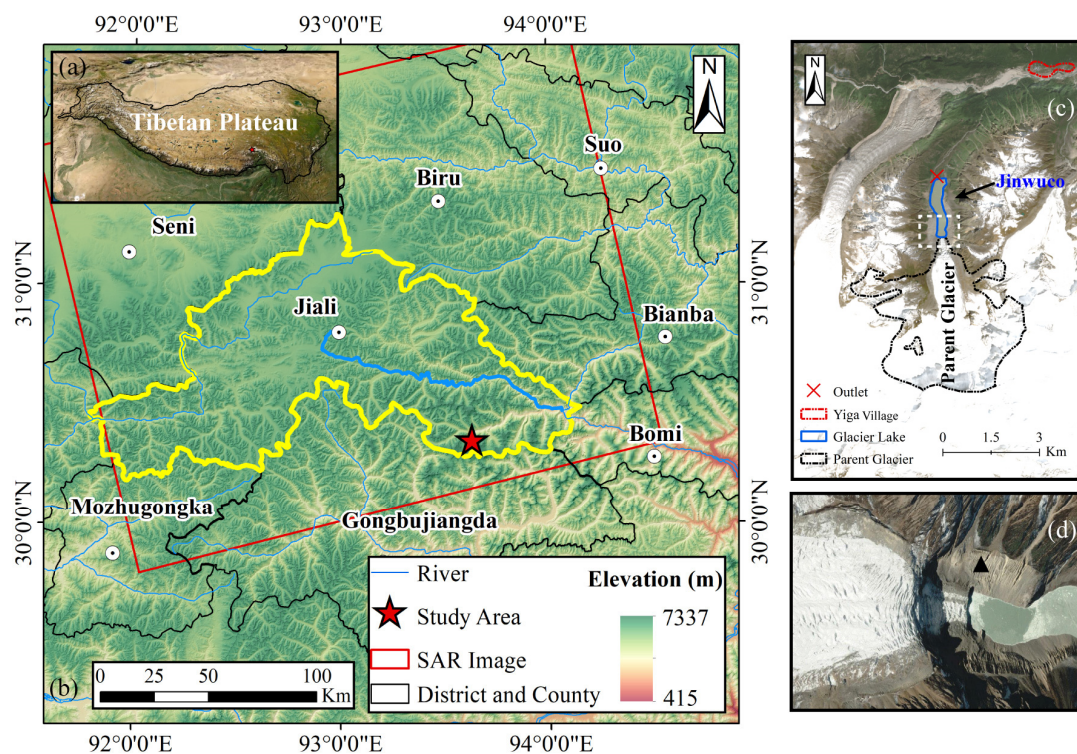

Figure 1. The location of Jinwuco Lake and its parent glacier. (**a**) Spatial position of the study region in the Tibetan Plateau. (**b**) A red rectangle denotes the coverage area of the image and the red pentagram represents the location of the study area. (**c**) Overall view of the glacier and glacial lake. (**d**) Local enlargement of the glacier terminus connected with the glacial lake from Google Earth. The black triangle is the selected radar backscatter feature point for analyzing the GLOF trigger factors.

Jinwuco is located in the southwest of the upper reaches of the Nidou Zangbo and is a glacier-fed lake, the largest glacial lake in the Nidou Zangbo basin [38]. In addition, the nearest village to Jinwuco, Yiga Village, is only 5.1 km away from the lake in a straight line. Before the disaster, the area of the glacial lake reached 0.56 km², and the area of the mother glacier was 7.9 km². The steep ice tongue at the end of the mother glacier is closely connected with the glacial lake. The lake's surface elevation is high in the south and low in the north, with an average elevation of 4461 m. The glacial lake is oriented north-south and appears as an irregular rectangle with a broader front and back and a narrower middle. Its linear length is approximately 1.8 km, its narrowest width is approximately 0.23 km, and its widest width is approximately 0.36 km. The mountain has a steep, east-west slope that averages 37.3° and 35.6° on each side, and it is either covered with vegetation or seasonal snow. A perennial drainage outlet with a width of roughly 13 m is located on the west side of the dam.

2.2. Datasets

In order to monitor surface deformation around the glacial lake before and after the GLOF, we collected 150 views of ascending Sentinel-1A images from March 2017 to February 2022. Simultaneously, the orbit state vector for each image was updated using

the precise orbit files released by ESA. The 1-arcsecond SRTM DEM was used to assist in the InSAR processing steps, such as co-registration between master and slave images, deduction of the topographic phase, and geocoding of the corresponding data. In addition, optical remote sensing images covering the study area from 1987 to 2020 with cloud content of less than 10% were collected to decode and identify the spatial and temporal evolution characteristics of the glacial lake and its surrounding surface. Meanwhile, the trigger analysis of GLOF events was carried out using ERA5 temperature data and GPM rainfall data from January 2017 to June 2020 [39,40]. The basic information of the data used in this paper are listed in Table 1.

Table 1. The basic information of the data used in this paper.

Data	Resolution	Date (yyyymmdd)	Number of Scenes	Purpose	Sources
Landsat5 TM	30 m	1987-11-08, 1990-06-25 1995-07-25, 2000-06-24 2005-09-06, 2010-10-06	6	Glacial lake mapping	https: //earthexplorer.usgs.gov (accessed on 2 March 2023)
Landsat8 OLI	30 m	2015-10-20	1	Glacial lake mapping	https: //earthexplorer.usgs.gov (accessed on 2 March 2023)
Sentinel-2A&B MSI	10 m	2019-09-26, 2020-05-01 2020-07-27	3	Glacial lake mapping	https: //scihub.copernicus.eu (accessed on 2 March 2023)
Sentinel-1A	Range 2.33 m, azimuth 13.96 m	2020-06-21, 2020-07-03	2	D-InSAR, POT	https: //search.asf.alaska.edu (accessed on 2 March 2023)
Sentinel-1A	Range 2.33 m, azimuth 13.96 m	2017-03-21–2022-02-23	150	Time-series displacement analysis	https: //search.asf.alaska.edu (accessed on 2 March 2023)
Precipitation	10 km	2017-01-01–2020-07-03	daily	Meteorological analysis	https://pmm.nasa.gov (accessed on 2 March 2023)
Temperature	10 km	2017-01-01–2020-07-03	daily	Meteorological analysis	https://cds.climate. copernicus.eu (accessed on 2 March 2023)

3. Methodology

Figure 2 is the workflow of this study. We obtain the long-term changes of the glacial lake and glacier terminus by multi-temporal remote sensing image interpretation. The POT and SBAS-InSAR methods based on Sentinel-1A SAR images are used to obtain the surface deformation around the lake. Finally, the corresponding monitoring results and meteorological data are combined to analyze the triggering factors of this GLOF event and identify potential landslide areas.
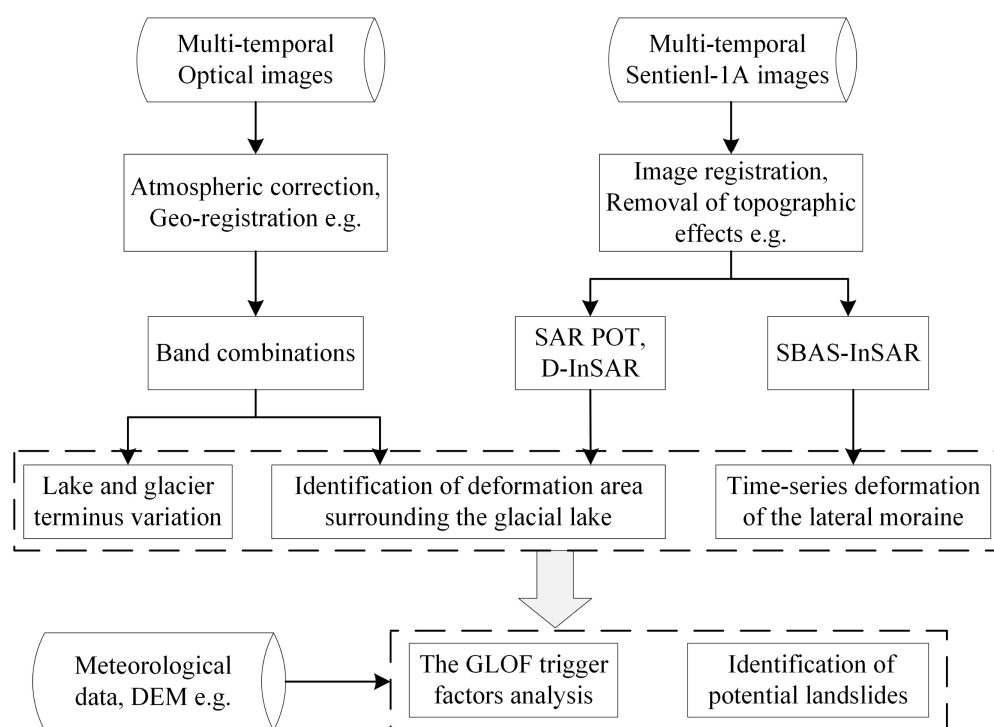
Figure 2. The workflow chart of this paper.

3.1. Extraction Methods of Glacial Lake and Glacier Information

Dynamic monitoring of glacial lake changes is critical for GLOF hazard studies [41–44], and its area change can reflect the overall trend of glacial lake expansion. The manual visual interpretation method was used to obtain the changes in the glacial lake area and glacier terminus position, which is simple to operate with relatively accurate results. To avoid the effect of cloud cover, we collected Landsat-5, Landsat-8, and Sentinel-2 images with less than 10% cloudiness. In addition, specific wave combination ratios are needed to highlight the differences between the various types of features in the images. The commonly used band combinations for glaciers and bare ground are the 543, 754 bands (corresponding to short-wave infrared (SWIR), near-infrared (NIR), and red bands) of Landsat-5 and Landsat-8 images and the 843 bands of Sentinel-2 (corresponding to NIR, red and green bands) [45,46]. Then, we used the Sentinel-2A image of September 26, 2019, as a reference image, and the remaining images were geo-registered. Ultimately, five inter-annual variations of the glacial lake and parent glacier terminus were counted and analyzed based on visual interpretation of lake boundaries. It should be noted that if the quality of the satellite images is severely affected by extreme weather, images from the same season in adjacent years can be used as substitutes.

3.2. SAR POT Processing

The pixel offset tracking based on SAR images is mainly implemented by two cross-correlation algorithms: coherence tracking and intensity tracking [47]. The former requires the existence of good coherence between the two scenes of SAR images and is suitable for regions with high coherence discontinuities. The latter has lower requirements for coherence and is suitable for regions with large displacements and poor coherence. Considering the complex natural geographical environment of the study area, we used the cross-correlation algorithm based on intensity tracking to monitor the displacement of the surface around the glacier lake in range and azimuth. All POT steps were processed using GMAMA software [48]. First, we deramped the registered SLC images for the azimuth phase ramp. Then, the offset fields in range and azimuth were estimated using the correlation function between SLC images. The image-matching window size was set to 128×128 with an oversampling factor of 2.

In addition, the finely registered SLC images were set with a 5:1 multi-look factor in range and azimuth, respectively, to improve their signal-to-noise ratio to suppress noise effectively, and the radar backscatter intensity of SAR images was calculated.

3.3. SBAS Processing

The SBAS-InSAR technique was used to acquire the time-series deformation of the surface around the glacial lake. The main principle is to set the optimal spatiotemporal baselines between SAR images and generate multiple differential interferometric pairs, and then use singular value decomposition to jointly solve the small baseline set to obtain the deformation time series of the whole period [49,50].

The interferometric pairs of the corresponding periods were severely decoherent due to the seasonal snow in the study area, and it is challenging to maintain good coherence even for interferometric pairs 12 days apart. Given this, we analyzed the coherence of all the interferometric pairs during the monitoring period and then eliminated the seriously decoherent image pairs. Ultimately, we divided all the images into five time periods according to the time of acquisition and selected the images mainly from June to October each year for data processing. All SBAS steps were processed using GMAMA software.

The temporal baseline and perpendicular thresholds were set to 50 days and 150 m to reduce the noise exhibited in the interferometric pairs due to spatio-temporal decoherence (Figure 3). We performed differential interference on the precisely registered single-look complex (SLC) images and then generated multiple interferometric pairs. To suppress the noise in the interferometric phase, we used an adaptive filtering function of 32 window sizes based on the power spectral density [51]. We used the minimum cost flow algorithm on a Delaunay triangular mesh to unwrap the wrapped interferometric phase [52]. Subsequently, the atmosphere screen associated with elevation was removed, and high-quality unwrapped differential interferograms were retained. Finally, the time series deformation information was inverted through singular value decomposition. The deformation away from the satellite is negative, and the deformation towards the satellite direction is positive in this paper.
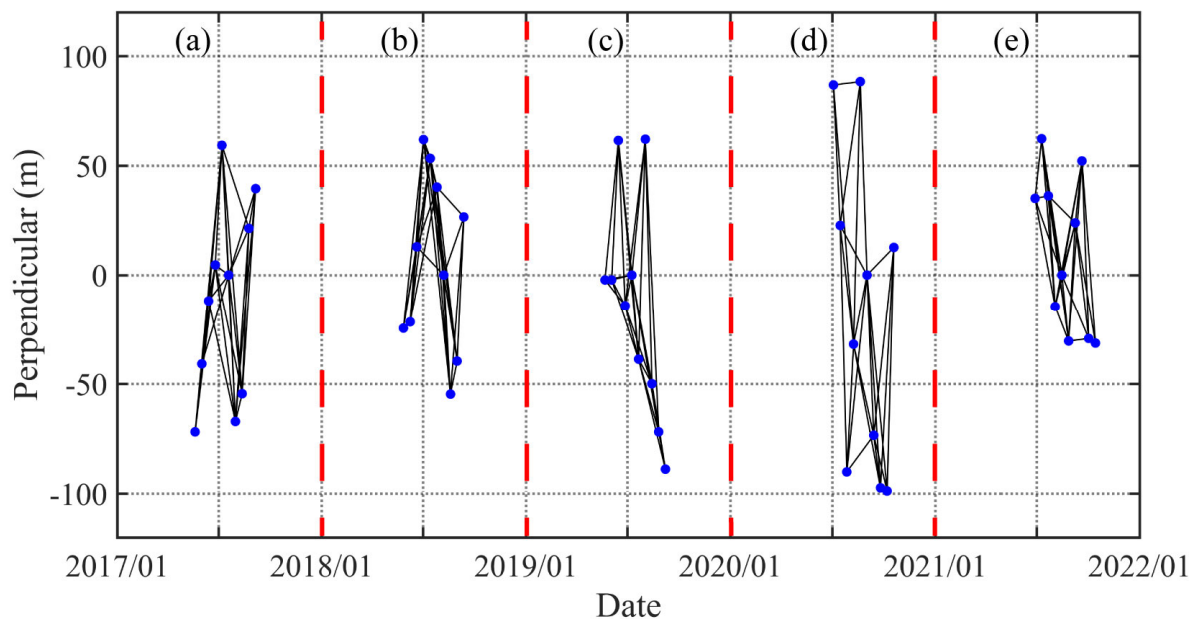

Figure 3. Spatial−temporal baseline for each period. (**a**–**e**) represent spatial−temporal baselines for different time periods, respectively.

4. Results and Analysis

4.1. Changes of Glacier Lake Area and Glacier Terminus in Recent 30 Years

We used optical images from 1987 to 2020 to interpret glacier terminus retreat and glacial lake area changes (Figure 4a). The historical images show that the glacier's terminus has continued to retreat since 1987, with a cumulative retreat distance of 700 m (Figure 4b). The retreat rate was relatively slow at 10 m/year before 2000 but accelerated to 30 m/year after 2000. Meanwhile, the glacial lake area expanded from 0.39 km^2 in 1987 to 0.56 km^2 before the disaster in 2020, with a cumulative increase of 0.17 km^2. Before 2005, the glacial lake expanded at a slower rate of 0.014 km^2·(5a)$^{-1}$, with a total expansion of 0.05 km^2. After 2005, the glacial lake area expanded at a faster rate of 0.055 km^2·(5a)$^{-1}$, with a total expansion of 0.11 km^2, accounting for 64.7% of the total increase (Figure 4b). The continuous retreat of glaciers supports the rapid expansion of glacial lakes. From the timing of the glacier terminus and glacial lake area entering accelerated change, we suggest that this may be related to the warming and humidifying climate of the region after 2000 [53,54].
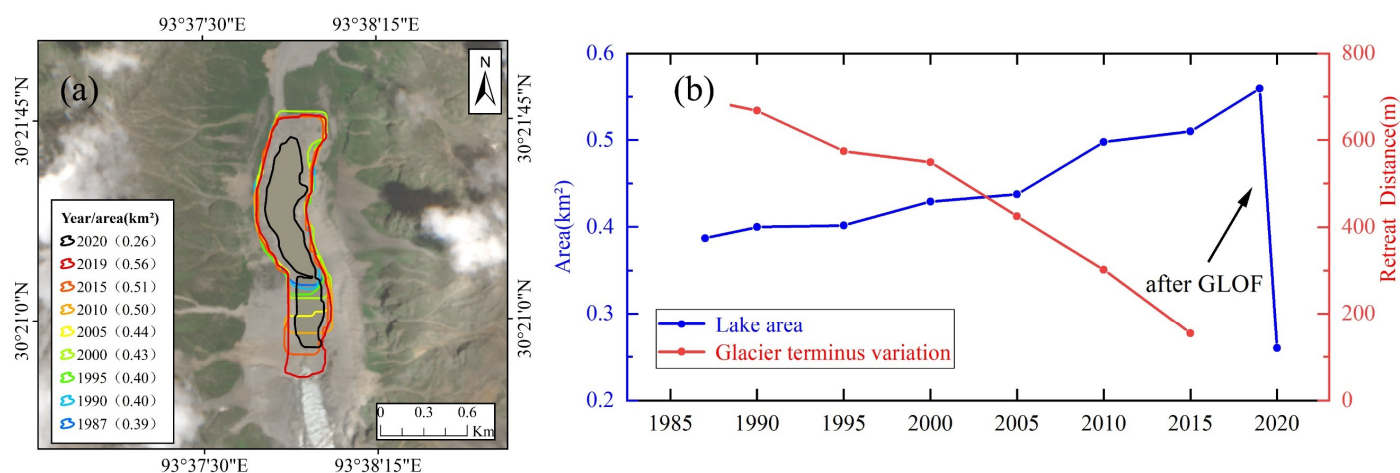

Figure 4. The changes of glacier lake area and glacier terminus. (**a**). the changes of the glacier lake area, (**b**). the changes of the glacier terminus.

After the glacial lake burst in June 2020, the lake water was quickly discharged, which caused the area of the glacial lake to decrease rapidly. The glacial lake area decreased from 0.56 km^2 to 0.26 km^2, which was 1.76 times greater than the increase in the glacial lake area (Figure 4b).

The rapid retreat of glaciers provides water and space for the expansion of glacial lakes. It exposes lateral moraines and mountain slopes initially covered by glaciers, which may reduce their stability [55,56]. Since these lateral moraine slopes are located above the glacial lake, a GLOF hazard may be induced in the event of instability. Therefore, we must further monitor their long-term deformation trends and capture anomalous deformation features (see Section 4.3). In summary, the glacier retreat and the glacier lake's continued expansion provide the primary conditions for this GLOF event, which has a similar development trend with the previous GLOFs [41,57].

4.2. Lateral Moraine and Glacier Lake Dam Deformation before and after the GLOF Event

In order to comprehensively understand the changes in glaciers, glacial lakes, and their surrounding surfaces in the short term before and after the occurrence of GLOF, we analyzed the areas of anomalous surface changes by combining optical images and deformations obtained by the D-InSAR and POT techniques. Optical images before and after the disaster show that the glacial lake area is significantly changing, and there are clear signs of the lateral moraine collapsing at the glacier's terminus at the junction of the glacier lake. The length and width of the slumping area are 680 m and 230 m, with an area of 0.1 km^2. The slip block is piled up directly in the glacial lake, and some mixed

ice and snow material is still at the back edge of the pile up (Figure 5). In the drainage area of the glacial lake, extensive surface damage may be caused by the rapid dumping of water after the outbreak of the glacial lake. During the rapid flow of flood water, the water continuously scours the ground surface around the outlet (e.g., mountain slopes, lateral moraine), causing massive damage to the surrounding terrain and accumulating large amounts of debris in the flood overflow area.
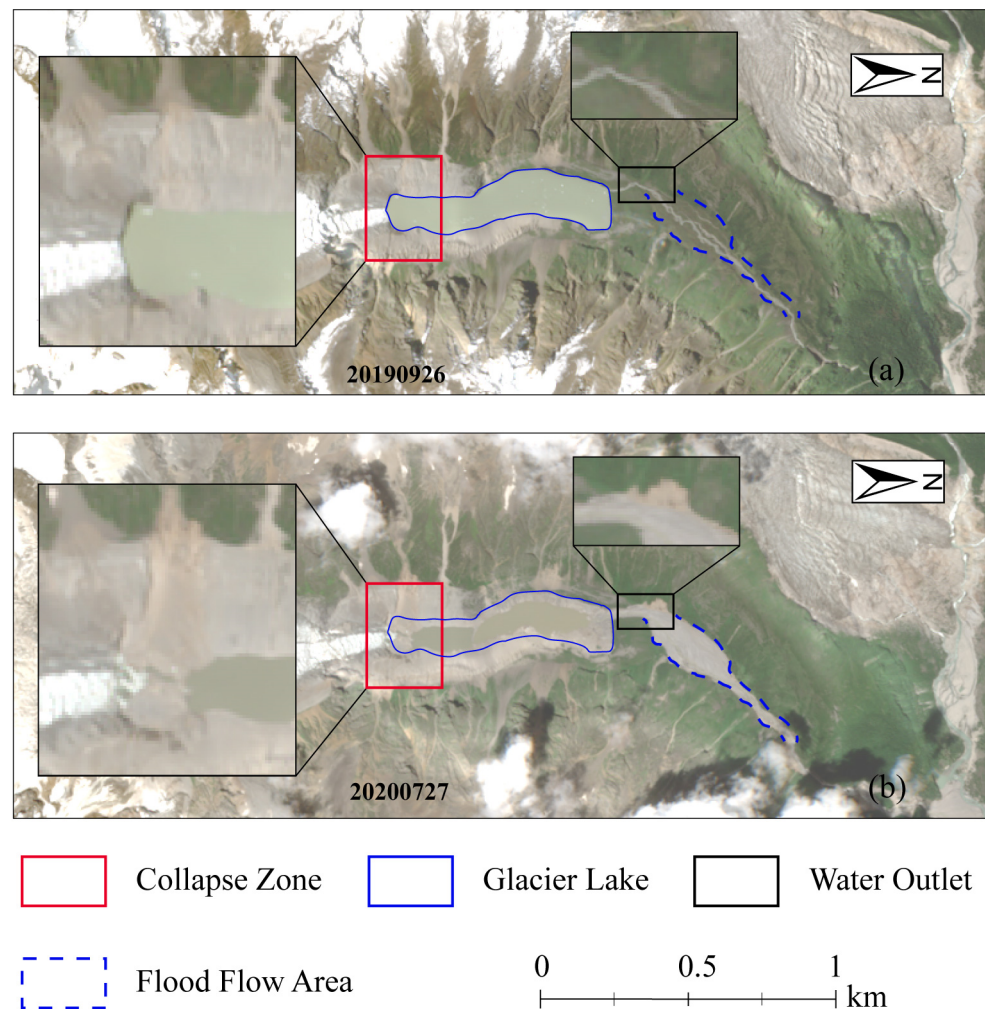

Figure 5. Optical remote sensing image recognition of lateral moraine collapse. The red rectangle represents the range of the slip zone. The blue polygon represents the boundary of the glacial lake. (**a**,**b**) represent the optical remote sensing images before and after the GLOF event. The black rectangle represents the lake's drainage outlet. The blue dashed line represents the flood flow area near the lake.

D-InSAR results obtained from Sentinel-1A images on 23 June 2020, and 3 July 2020, show that the deformation variables in most of the area around the glacial lake before and after the occurrence of GLOF (25 June 2020) are in the range of -10–5 mm, which indicates that most of the area is in a relatively stable state (Figure 6). However, there are three prominent deformation zones on the upper slope of the lateral moraine landslide area, with a maximum deformation of -40 mm. The deformation results in the landslide region could not be obtained due to the severe decoherence of the interference phase caused by the large gradient deformation in the surface damage region.
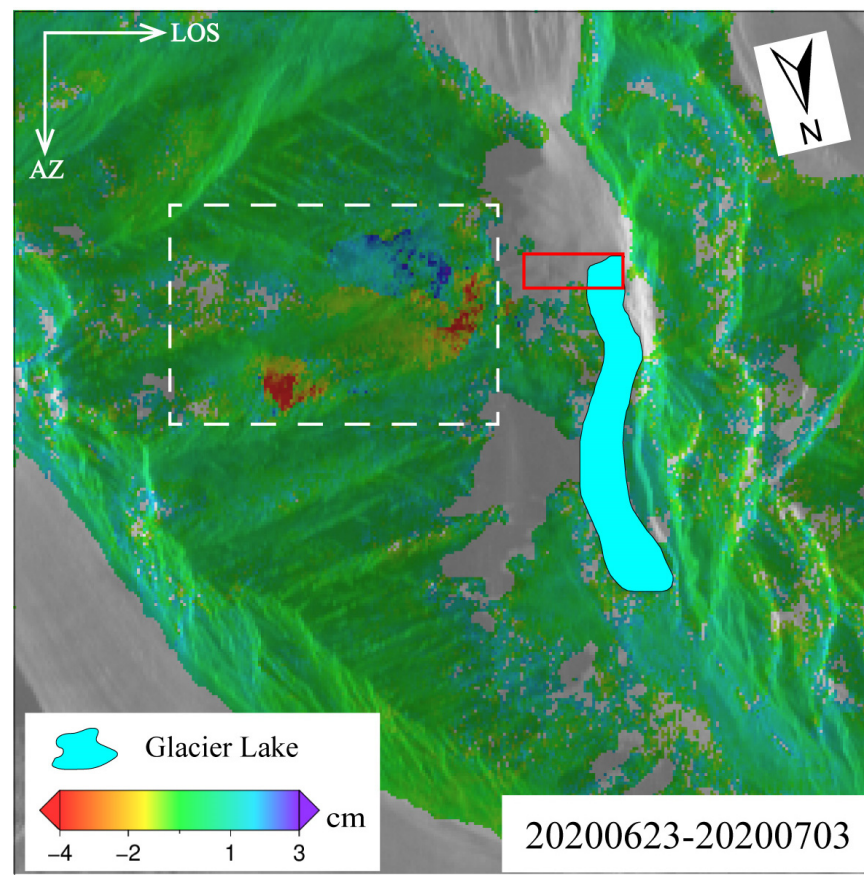
Figure 6. The results of the surface deformation around the glacial lake are shown in a radar coordinate. It is important to note that its direction of which is shown approximately upside down compared to the direction of the geographical coordinates. The white dashed box indicates the deformation area, red rectangle represents the collapse zone and the light blue polygon represents the Jinwuco lake.

Because of this, we used the intensity information of images from the same period and POT technology to obtain the deformation results of the surface damage zone. The corresponding results show that there are significant deformation signals near both the collapse and drainage areas, as shown in Figure 7, where a positive value (blue color) indicates a movement toward the sensor, and a negative value (red color) indicates movement away from the sensor.

Combining the deformation results in range and azimuth, it can be seen that the collapse area mainly moves in the northeast direction, and the maximum deformation reaches −60 m. Deposits mainly move along the southeast direction, with a maximum deformation of 55 m. This is consistent with our optical image interpretation that the slumping area moves downward along the slope, and the accumulation is mainly located near the glacier's terminus. The displacement of the drainage area in the distance direction is mainly toward the direction of the satellite, and the maximum deformation is 55 m. However, its deformation characteristics in the azimuthal direction are divided by the location of moraine dams, which show opposite deformation signals. The inner side of the glacial lake behaves away from the satellite direction. In contrast, the outer side of the glacial lake behaves close to the satellite direction, with a maximum deformation variable of 88 m. Optical images before and after the disaster show that the moraine dam was not destroyed, but the post-disaster drainage of the glacial lake was significantly larger. Part of the material in the lake was discharged from the breach with the flood and accumulated outside the dam body, while the other part accumulated inside the dam body.

The above analysis not only shows the reliability of the POT results, but we also found nearly synchronous lateral moraine collapse with the glacial lake outburst, which provides support for the subsequent discussion of the triggering factors of GLOF (see Section 5.1).
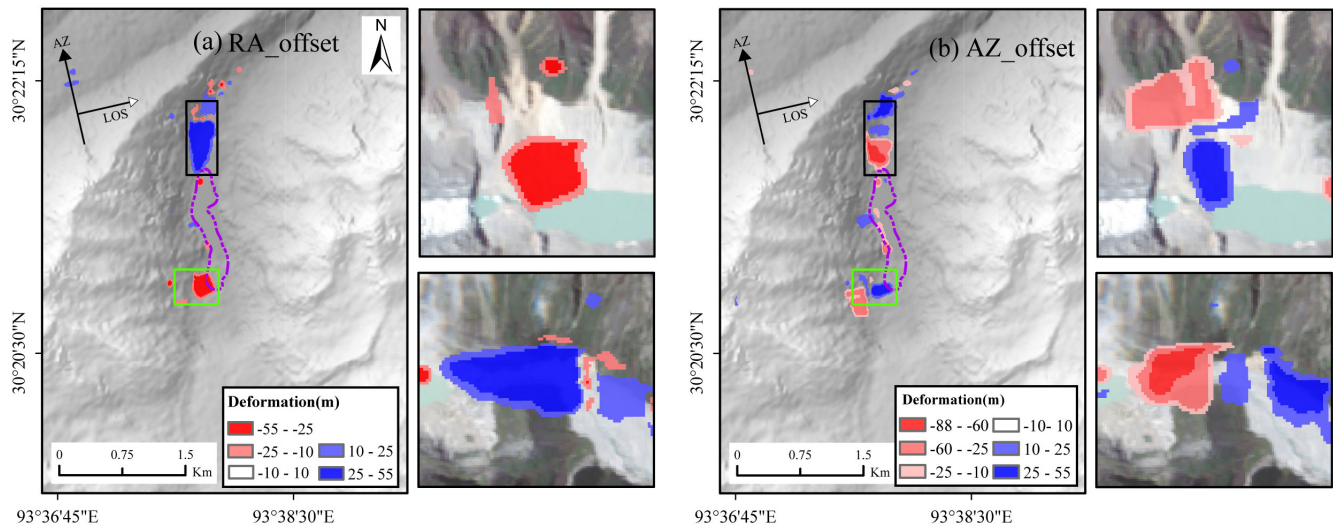

Figure 7. The lateral moraine and glacier lake dam deformation before and after the GLOF event. The purple dotted line represents the extent of the lake. (**a**,**b**) are the range and azimuthal deformation of the ground surface, respectively.

4.3. Surface Deformation Processes around the Glacial Lake from 2017 to 2021

In order to comprehensively assess the surface deformation processes in the collapse zone and other areas around the glacial lake, and to capture the possible anomalous deformation signals on the surface around the glacial lake before and after the GLOF event, we obtained the surface deformation results from 2017 to 2021 using the SBAS-InSAR technique. In this paper, the InSAR deformation results for equal time intervals for different years were obtained over a time span of 120 days. Figure 8 shows the results of the surface deformation around the glacial lake for different years, where positive values represent the direction close to the satellite line of sight and negative values represent the direction far from the satellite line of sight.

4.3.1. Surface Deformation Processes around the Glacial Lake before the GLOF Event

The SBAS-InSAR results show that during the monitoring period before GLOF (2017–2019), the cumulative deformation of most surface areas around the glacial lake before was in the range of −10–10 mm, indicating that most areas were stable. There are apparent surface deformation signals in the slump zone, and the accumulated deformation was −52–0 mm during the monitoring period. There are also three mountain slopes with obvious deformation, which are the P1, P3, and P4 areas. We found that the P2 area near the slump area had the most significant deformation in 2017, with a maximum deformation of −52 mm during the monitoring period. In comparison, the cumulative maximum deformation in the P2 region was −32 mm and −43 mm in 2018 and 2019, respectively.
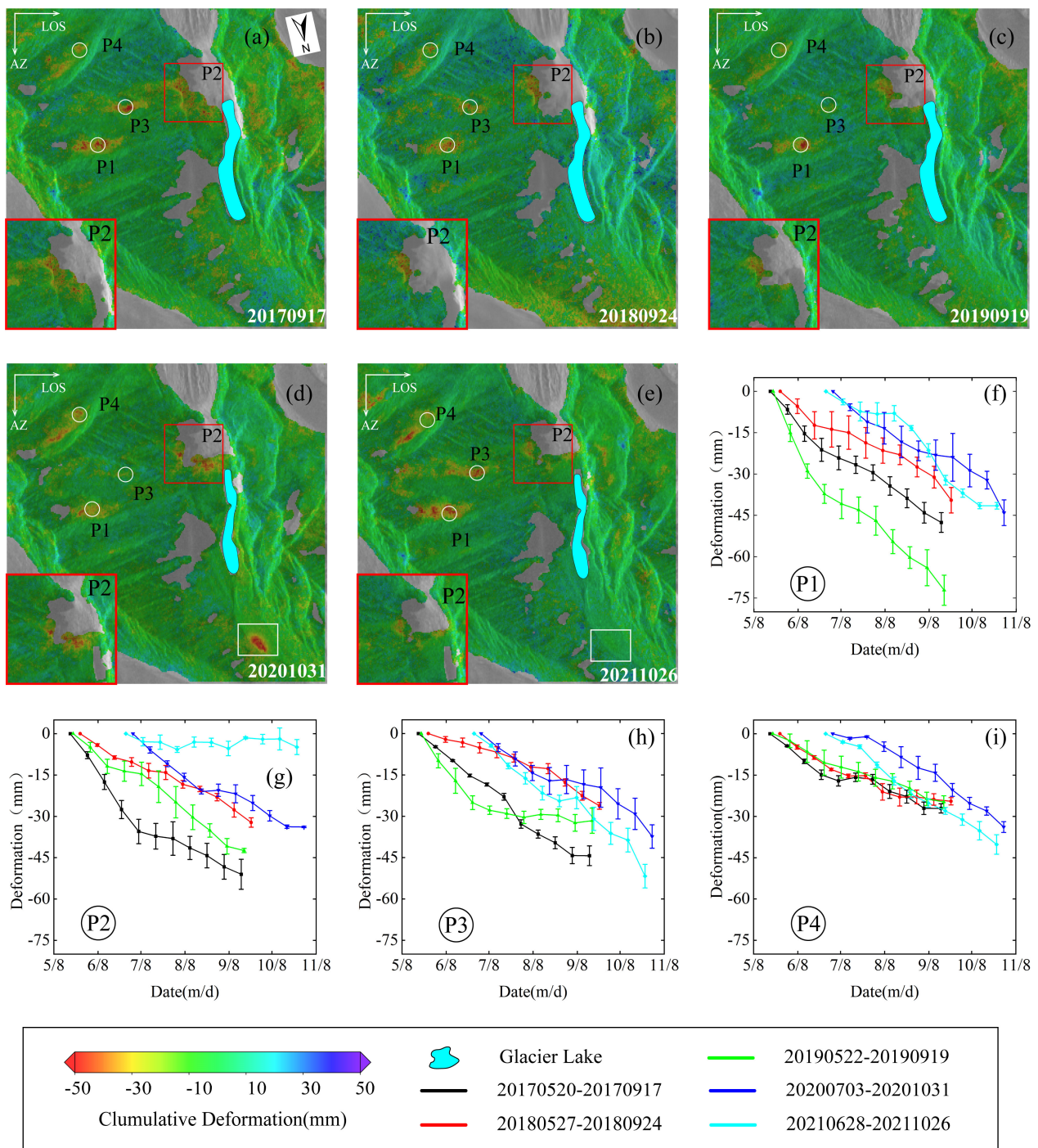
Figure 8. Surface deformation monitoring results of the mountains around the glacial lake. (**a**–**e**) represent the cumulative deformation of different monitoring cycles in radar coordinate. P1–P4 are the selected typical deformation areas. (**f**–**i**) represent the time series deformation results for each region.

The area and magnitude of surface deformation areas show spatial heterogeneity over different observation periods. The surface deformation values and areas were relatively larger in 2017 over the same observation period. The P3 area directly above the slump zone also exhibited the greatest deformation extent and magnitude in 2017, with a maximum cumulative deformation of −45 mm. The deformation of the oblique upper P1 region in the P3 region was the largest in 2019. However, its deformation area is smaller than in previous years, and the maximum deformation is −72 mm. The cumulative deformation of the P4

area is relatively close in each monitoring period before the disaster, and the cumulative deformation is smaller than the P1, P2, and P3 zones. The maximum deformation was only −27 mm during the monitoring period. The surface time series deformation sequence results show that the four deformation areas have evident deformation intensification in the observation period, and the trend of deformation intensification in 2017 and 2019 is the most significant. By calculating the average deformation rate of P1–P4 from 207 to 2019, we found that the deformation rate in 2017 was −14 mm/month. The deformation rate in 2019 was −14 mm/month, significantly higher than the average in 2018 was −10 mm/month. This indicates that the lateral moraine slope had experienced multiple deformation acceleration stages before the disaster.

In general, the range of deformation and cumulative deformation variables was relatively large in 2017, followed by 2019, and 2018 showed minor cumulative deformation in all deformation zones. The anomalous changes in surface deformation before GLOF were mainly influenced by climatic factors (see Section 5.1).

4.3.2. Surface Deformation Processes around the Glacial Lake after the GLOF Event

In 2020, after the GLOF occurred and severe surface damage occurred in the landslide area, the remaining surface deformation areas also changed accordingly. The deformation range near the slump area increased significantly, and obvious surface deformation signals were observed at the trailing edge of the slump area. However, the deformation magnitude in this area was lower than that in 2017 and 2019 before the disaster, and the maximum cumulative deformation was −32 mm (Figure 8g). The main reason for the increase in the deformation range in this area is the influence of the lateral moraine collapse. The slope movement will destroy the surface stability of adjacent areas, and loose deposits are prone to displacement under the influence of rainfall, meltwater, and other factors. In 2021, after the disaster, the cumulative surface deformation and deformation range around the landslide area decreased significantly, and the overall deformation was in the range of −5–0 mm, indicating that the area was stable during this monitoring period. We believe this is after the violent sliding, the lateral moraine collapse, and the body deformation. It tends to stop as the center of gravity decreases, the declining energy decreases, the anti-slip force increases, the displacement speed slows down, and the anti-slip force gradually decreases [58]. It is worth noting that the surface around the lake was affected by snow in winter, resulting in inferior interferometric quality between the images and the inability to effectively separate the deformation signal, so we cannot be more precise about when the collapse zone stabilized. The surface around the collapse zone may have stabilized between November 2020 and June 2021, or it may begin to stabilize gradually only in the second year after the disaster. However, in any case, in the second year of monitoring, the collapse zone is stable from the InSAR deformation results we obtained. At the same time, we found a significant surface deformation in the GLOF flow area in 2020, and the maximum cumulative surface deformation is −58 mm. Comparing optical images reveals that the area is in the middle of the accumulation zone. However, one year after the GLOF (2021), no significant surface deformation was monitored in the region, indicating that the region became relatively stable in the second year after the disaster. Therefore, the deformation is mainly affected by the short-term impact of the fast-moving glacial lake outburst flood and does not fundamentally impact the mountains around the region.

In addition, there is still apparent surface deformation after the disaster in the P1, P3, and P4 regions before the GLOF. We found that in addition to the slope near the lateral moraine collapse zone, it tends to be stable in 2021 after the disaster. The deformation magnitude and deformation range of the P3 and P4 regions have increased during the post-disaster monitoring period, and the maximum cumulative deformation is −51 mm and −40 mm, respectively. Moreover, although the deformation magnitude of the P1 region does not increase significantly, its deformation range tends to expand. Similar to the analysis above, this slip movement may have also influenced this.

5. Discussion

5.1. Triggering Factors of GLOF

In general, sustained summer heat and rainfall promote glacier melting, which provides a large amount of water for the glacial lake [59]. Especially in the case of underground outflow, the water content of the surface increases through infiltration into the slope and gradually affects the stability of the slope [60]. In addition, high-intensity precipitation will aggravate the above situation and induce lateral moraine collapse and ice avalanches or directly increase the volume of the glacial lake, leading to GLOF events. [23]. To understand the meteorology of the GLOF events and their impacts on slope deformation and GLOF events, we counted and plotted daily average rainfall, monthly precipitation, and temperature data for the study area from 2017 to 2020 (Figure 9).
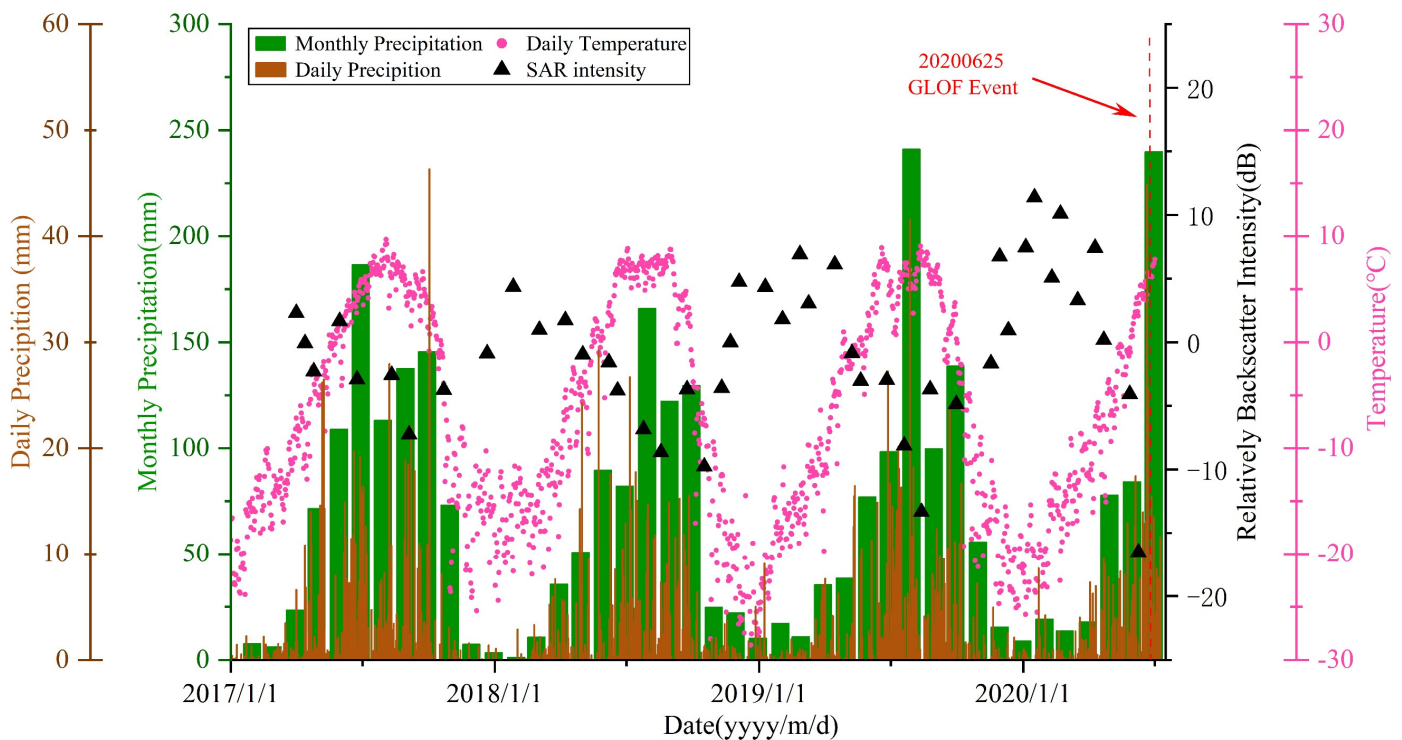

Figure 9. Correlation analysis between ground temperature, precipitation and relatively backscatter intensity of landslide for black triangle marked in Figure 1d.

According to the temperature data, the highest temperatures in the study area occur between June and September each year, when the average daily temperature is above 0 °C. During this period, the glaciers are melting, and the frozen period of the glacial lakes is over. In the year 2020, before the GLOF, the overall temperature was continuously warming, with the temperature reaching its peak in June before the disaster. There are large interannual fluctuations in precipitation in the study area and seasonal fluctuations, with low precipitation in winter and high precipitation in summer. The cumulative monthly rainfall in June 2020 was up to 240 mm, the most considerable monthly seasonal rainfall since 2018. Persistent rainfall existed throughout June, and 45 mm of rainfall was observed four days before the GLOF event, which was the maximum daily rainfall for the month. It is not difficult to find evidence that lateral moraine collapse and GLOF occurred after warm and unusually wet weather. Given a period of relatively dry and warm days prior to the GLOF event, the subsequent gradual snowmelt that provided runoff to the watershed could provide a plausible explanation for the lag between this heavy precipitation event, the onset of the landslide, and the outburst flood. However, the current results still need to be apparent for the relationship between the lateral moraine collapse and GLOF. It is

difficult to determine whether the lateral moraine slump leads to GLOF or whether the lateral moraine slump is induced after GLOF occurs.

In view of this, we analyzed the temporal deformation pattern and the relationship between deformation and rainfall response in the lateral moraine and other surface deformation areas. According to the deformation results and meteorological data for P1–P4 from 2017 to 2021, it is found that cumulative deformation variables in the deformation zone are significantly more extensive and more susceptible to significant periods of deformation acceleration during rainy seasons with high accumulated precipitation, and the presence of peak precipitation, such as in 2017 and 2019 and 2020. In addition, the significant deformation trend of the lateral moraine slope for three consecutive rainy seasons indicates that it may be on the verge of instability, which makes it vulnerable to landslide under rainfall conditions, and this conclusion is consistent with the findings of Guo et al. (2020) [61]. Existing studies show that persistent and high-intensity precipitation increases surface water content mainly through infiltration deformation, which increases slope instability [62]. Considering the scorching and humid climate in 2020, glacier meltwater would affect soil moisture and precipitation. Therefore, we extracted the time-series radar backscatter intensity around the lateral moraine collapse zone using SAR intensity deformation to characterize the changes in soil moisture (Figure 9). The radar backscatter intensity prior to the onset of GLOF was at the lowest on record, indicating that this period experienced extremely wet soil moisture, which would favor the onset of instability in the lateral moraine. Considering the direction of movement of the lateral moraine slip and the accumulation area mainly located in the junction area between the collapse area and the glacier terminus (see Section 4.2), we believe that the continuous precipitation and peak rainfall in 2020 caused the lateral moraine slip in the first place. The lateral moraine slip entered the glacial lake and stirred up surge waves, which led to the outburst flood. Our conclusions from the deformation patterns of glacial meltwater, rainfall, soil moisture changes, and lateral moraine landslides are consistent with Zheng et al. (2021) [14]. Nevertheless, we put more emphasis on the fact that glacial meltwater and rainfall can influence the stability of lateral moraine landslides and thus induce GLOF by increasing the surface water content in a semi-quantitative manner.

In addition, Yang et al. (2022) suggested the possibility of ice avalanche-induced GLOF [46]. We found a partial ice mixture in the accumulation formed by the lateral moraine slip in the optical image interpretation. However, by comparing the optical images of the glacier terminus for many years and the changes of the glacier terminus before the disaster, no significant new ice crevices appeared before the disaster, and the glacier terminus did not show significant changes before GLOF. Therefore, we believe that the ice and snow mixture in the accumulation area, which collided with the end of the glacier during the collapse of the lateral moraine and carried part of the ice and snow material; we can basically exclude the possibility that an ice avalanche induced GLOF.

In summary, this study suggests that GLOF occurred during a warm and unusually wet period, when high temperatures promoted glacial ablation and provided runoff to the watershed, and sustained and intense rainfall further increased surface water content and reduced the stability of lateral moraines. Ultimately, a lateral moraine slump occurred at the glacial lake's junction and the glacier's terminus. Due to the vast kinetic energy and potential energy carried by the rapid displacement, the source of the slumped body quickly stirred up surges after entering the glacial lake. It caused overtopping, which eventually led to GLOF.

5.2. Surface Deformation around Glacial Lakes and Potential GLOF Risk

Considering the intensification of southeast Tibet's warm and humid climate in recent years, the possibility of extreme weather increases in the future [63]. It is foreseeable that the glacier will continue to retreat and melt under such climate conditions, and more glacial lakes may expand further. In addition, with time, the glacial lake may also return to its original volume after the outburst, becoming a potentially dangerous glacial lake that may be affected external driving forces, and GLOF events may occur again. Exposed lateral

moraines after glacier retreat will be less stable after losing glacier support. The possibility of slippage in the less stable lateral moraine will gradually increase in the hot and humid climate. Consequently, GLOF events caused by external factors such as lateral moraine landslides and ice avalanches require our further attention. According to SBAS-InSAR results, three distinct areas of surface deformation still exist around the glacial lake, and the cumulative deformation increases significantly during the rainy season (see Section 4.3). There is a possibility of destabilization in these regions under future climate states. Since these three deformation zones are higher in height relative to the glacial lake surface than the 2020 collapse zone, they have greater potential energy. When it collapses over a large area, the potential energy is converted into kinetic energy, which creates a source of high-speed motion in the glacial lake that may stir up an enormous surge, causing a larger GLOF than the one in June 2020. This will seriously affect the surrounding infrastructure and people's safety; for these areas, we need to strengthen the monitoring means to avoid or mitigate the possible impact of the disaster.

6. Conclusions

This paper systematically analyzes the spatial and temporal evolution characteristics and triggering factors of GLOF disasters by combining multi-temporal optical remote sensing interpretation, SAR/InSAR surface deformation monitoring, meteorological data, and soil moisture changes. The main results are summarized as follows:

(1) Multi-temporal optical remote sensing interpretation results show that not only did the glacier's terminus retreat by about 700 m from 1987 to 2020 before the disaster, but also the area of the glacial lake expanded by 0.17 km^2. The reduction of the glacial lake area after the GLOF event was 1.76 times the total increase before the disaster. The lateral moraine collapse located on the west side of the glacial lake and near the lake drainage outlet is monitored by the POT technique. The maximum deformation in range is 55 m and in azimuth is 88 m.

(2) The time series of InSAR results from 2017 to 2019 indicate that the surrounding area of the landslide area was in a state of deformation for a long time before the disaster, with a maximum cumulative deformation of −52 mm. The landslide area gradually stabilized after the disaster, and the accumulated deformation is less than −5 mm in the monitoring period of 2021. In addition, InSAR results show that three areas still exhibited significant deformation during the post-disaster monitoring period. The accumulated deformation is more remarkable than −35 mm, with the possibility of destabilization, which requires further attention.

(3) Meteorological factors are crucial contributors to this disaster. High temperatures promote glacial melt and provide runoff to the watershed, and continuous and intense rainfall further increases the surface water content and reduces the stability of the lateral moraine. Finally, at the junction of the glacial lake and the end of the glacier occurred the lateral moraine slip, the source of the slip body because of carrying tremendous kinetic energy, into and at the rapid and its surge triggered diffuse top, and finally led to the GLOF.

The above results show that the combination of active and passive remote sensing technology to carry out GLOF hazard research can accurately obtain its spatial and temporal evolution characteristics and triggering factors, which will help further understand GLOF events due to lateral moraine landslides. As regional warming and humidification intensify, rapid glacier retreat and melting will further lead to the instability of lateral moraines and glacial lakes. GLOF disasters similar to Jinwuco will require more attention in the future. This study helps to improve our ability to assess and manage GLOF disaster risk and establish a scientific and practical early warning and forecasting system to reduce and avoid the impact of GLOF.

References

1. Zhao, F.Y.; Long, D.; Li, X.D.; Huang, Q.; Han, P.F. Rapid glacier mass loss in the Southeastern Tibetan Plateau since the year 2000 from satellite observations. *Remote Sens. Environ.* **2022**, *270*, 112853. [CrossRef]
2. Ji, Q.; Yang, T.-b.; Li, M.-q.; Dong, J.; Qin, Y.; Liu, R. Variations in glacier coverage in the Himalayas based on optical satellite data over the past 25 years. *CATENA* **2022**, *214*, 106240. [CrossRef]
3. Wang, X.; Guo, X.; Yang, C.; Liu, Q.; Wei, J.; Zhang, Y.; Liu, S.; Zhang, Y.; Jiang, Z.; Tang, Z. Glacial lake inventory of high-mountain Asia in 1990 and 2018 derived from Landsat images. *Earth Syst. Sci. Data* **2020**, *12*, 2169–2182. [CrossRef]
4. Shugar, D.H.; Burr, A.; Haritashya, U.K.; Kargel, J.S.; Watson, C.S.; Kennedy, M.C.; Bevington, A.R.; Betts, R.A.; Harrison, S.; Strattman, K. Rapid worldwide growth of glacial lakes since 1990. *Nat. Clim. Chang.* **2020**, *10*, 939–945. [CrossRef]
5. Liu, J.-J.; Cheng, Z.-L.; Su, P.-C. The relationship between air temperature fluctuation and Glacial Lake Outburst Floods in Tibet, China. *Quat. Int.* **2014**, *321*, 78–87. [CrossRef]
6. Legg, S. IPCC, 2021: Climate Change 2021-the Physical Science basis. *Interaction* **2021**, *49*, 44–45.
7. Sattar, A.; Goswami, A.; Kulkarni, A.V.; Emmer, A.; Haritashya, U.K.; Allen, S.; Frey, H.; Huggel, C. Future Glacial Lake Outburst Flood (GLOF) hazard of the South Lhonak Lake, Sikkim Himalaya. *Geomorphology* **2021**, *388*, 107783. [CrossRef]
8. Che, Y.; Wang, S.; Wei, Y.; Pu, T.; Ma, X. Rapid changes to glaciers increased the outburst flood risk in Guangxieco Proglacial Lake in the Kangri Karpo Mountains, Southeast Qinghai-Tibetan Plateau. *Nat. Hazards* **2022**, *110*, 2163–2184. [CrossRef]
9. Tiberti, R.; Buscaglia, F.; Callieri, C.; Rogora, M.; Tartari, G.; Sommaruga, R. Food Web Complexity of High Mountain Lakes is Largely Affected by Glacial Retreat. *Ecosystems* **2019**, *23*, 1093–1106. [CrossRef]
10. Jouberton, A.; Shaw, T.E.; Miles, E.; McCarthy, M.; Fugger, S.; Ren, S.; Dehecq, A.; Yang, W.; Pellicciotti, F. Warming-induced monsoon precipitation phase change intensifies glacier mass loss in the southeastern Tibetan Plateau. *Proc. Natl. Acad. Sci. USA* **2022**, *119*, e2109796119. [CrossRef]
11. Che, Y.; Zhang, M.; Li, Z.; Li, H.; Wang, S.; Sun, M.; Zha, S. Glacier mass-balance and length variation observed in China during the periods 1959–2015 and 1930–2014. *Quat. Int.* **2017**, *454*, 68–84. [CrossRef]
12. Sun, M.; Liu, S.; Yao, X.; Li, L. The cause and potential hazard of glacial lake outburst flood occurred on July 5, 2013 in Jiali County, Tibet. *J. Glaciol. Geocryol.* **2014**, *36*, 158–165.
13. Liu, J.; Zhang, J.; Gao, B.; Li, Y.; Li, M.; Wujin, D.; Zhou, L. An overview of glacial lake outburst flood in Tibet, China. *J. Glaciol. Geocryol.* **2019**, *41*, 1335–1347.
14. Zheng, G.X.; Mergili, M.; Emmer, A.; Allen, S.; Bao, A.M.; Guo, H.; Stoffel, M. The 2020 glacial lake outburst flood at Jinwuco, Tibet: Causes, impacts, and implications for hazard and risk assessment. *Cryosphere* **2021**, *15*, 3159–3180. [CrossRef]
15. Nie, Y.; Liu, Q.; Wang, J.; Zhang, Y.; Sheng, Y.; Liu, S. An inventory of historical glacial lake outburst floods in the Himalayas based on remote sensing observations and geomorphological analysis. *Geomorphology* **2018**, *308*, 91–106. [CrossRef]
16. Hu, J.; Yao, X.; Duan, H.; Zhang, Y.; Wang, Y.; Wu, T. Temporal and Spatial Changes and GLOF Susceptibility Assessment of Glacial Lakes in Nepal from 2000 to 2020. *Remote Sens.* **2022**, *14*, 5034. [CrossRef]
17. Wang, S.; Che, Y.; Xinggang, M. Integrated risk assessment of glacier lake outburst flood (GLOF) disaster over the Qinghai–Tibetan Plateau (QTP). *Landslides* **2020**, *17*, 2849–2863. [CrossRef]
18. Liu, Q.; Guo, W.; Nie, Y.; Liu, S.; Xu, J. Recent glacier and glacial lake changes and their interactions in the Bugyai Kangri, southeast Tibet. *Ann. Glaciol.* **2016**, *57*, 61–69. [CrossRef]

19. Nie, Y.; Liu, W.; Liu, Q.; Hu, X.; Westoby, M.J. Reconstructing the Chongbaxia Tsho glacial lake outburst flood in the Eastern Himalaya: Evolution, process and impacts. *Geomorphology* **2020**, *370*, 107393. [CrossRef]

20. Hock, R.; Rasul, G. High Mountain Areas. In *The Ocean and Cryosphere in a Changing Climate*; Cambridge University Press: Cambridge, UK, 2022; pp. 131–202. [CrossRef]

21. Yao, X.; Liu, S.; Sun, M.; Wei, J.; Guo, W. Volume calculation and analysis of the changes in moraine-dammed lakes in the north Himalaya: A case study of Longbasaba lake. *J. Glaciol.* **2017**, *58*, 753–760. [CrossRef]

22. Klimeš, J.; Novotný, J.; Novotná, I.; de Urries, B.J.; Vilímek, V.; Emmer, A.; Strozzi, T.; Kusák, M.; Rapre, A.C.; Hartvich, F.; et al. Landslides in moraines as triggers of glacial lake outburst floods: Example from Palcacocha Lake (Cordillera Blanca, Peru). *Landslides* **2016**, *13*, 1461–1477. [CrossRef]

23. Wilson, R.; Harrison, S.; Reynolds, J.; Hubbard, A.; Glasser, N.F.; Wündrich, O.; Iribarren Anacona, P.; Mao, L.; Shannon, S. The 2015 Chileno Valley glacial lake outburst flood, Patagonia. *Geomorphology* **2019**, *332*, 51–65. [CrossRef]

24. Wang, W.; Yao, T.; Yang, W.; Joswiak, D.; Zhu, M. Methods for assessing regional glacial lake variation and hazard in the southeastern Tibetan Plateau: A case study from the Boshula mountain range, China. *Environ. Earth Sci.* **2012**, *67*, 1441–1450. [CrossRef]

25. Ahmed, R.; Wani, G.F.; Ahmad, S.T.; Sahana, M.; Singh, H.; Ahmed, P. A Review of Glacial Lake Expansion and Associated Glacial Lake Outburst Floods in the Himalayan Region. *Earth Syst. Environ.* **2021**, *5*, 695–708. [CrossRef]

26. Zhang, T.; Wang, W.; Gao, T.; An, B.; Yao, T. An integrative method for identifying potentially dangerous glacial lakes in the Himalayas. *Sci. Total Environ.* **2022**, *806*, 150442. [CrossRef]

27. Wang, W.; Yao, T.; Yang, X. Variations of glacial lakes and glaciers in the Boshula mountain range, southeast Tibet, from the 1970s to 2009. *Ann. Glaciol.* **2011**, *52*, 9–17. [CrossRef]

28. Wangchuk, S.; Bolch, T.; Zawadzki, J. Towards automated mapping and monitoring of potentially dangerous glacial lakes in Bhutan Himalaya using Sentinel-1 Synthetic Aperture Radar data. *Int. J. Remote Sens.* **2019**, *40*, 4642–4667. [CrossRef]

29. Dini, B.; Daout, S.; Manconi, A.; Loew, S. Classification of slope processes based on multitemporal DInSAR analyses in the Himalaya of NW Bhutan. *Remote Sens. Environ.* **2019**, *233*, 111408. [CrossRef]

30. Cai, J.; Zhang, L.; Dong, J.; Wang, C.; Liao, M. Polarimetric SAR pixel offset tracking for large-gradient landslide displacement mapping. *Int. J. Appl. Earth Obs.* **2022**, *112*, 102867. [CrossRef]

31. Choe, B.-H.; Samsonov, S.; Jung, J. 3D SAR Speckle Offset Tracking Potential for Monitoring Landfast Ice Growth and Displacement. *Remote Sens.* **2021**, *13*, 2168. [CrossRef]

32. Chen, B.; Mei, H.; Li, Z.; Wang, Z.; Yu, Y.; Yu, H. Retrieving Three-Dimensional Large Surface Displacements in Coal Mining Areas by Combining SAR Pixel Offset Measurements with an Improved Mining Subsidence Model. *Remote Sens.* **2021**, *13*, 2541. [CrossRef]

33. Li, M.; Zhang, L.; Shi, X.; Liao, M.; Yang, M. Monitoring active motion of the Guobu landslide near the Laxiwa Hydropower Station in China by time-series point-like targets offset tracking. *Remote Sens. Environ.* **2019**, *221*, 80–93. [CrossRef]

34. Fan, X.; Xu, Q.; Alonso-Rodriguez, A.; Subramanian, S.S.; Li, W.; Zheng, G.; Dong, X.; Huang, R. Successive landsliding and damming of the Jinsha River in eastern Tibet, China: Prime investigation, early warning, and emergency response. *Landslides* **2019**, *16*, 1003–1020. [CrossRef]

35. Liu, X.J.; Zhao, C.Y.; Zhang, Q.; Lu, Z.; Li, Z.H. Deformation of the Baige Landslide, Tibet, China, Revealed Through the Integration of Cross-Platform ALOS/PALSAR-1 and ALOS/PALSAR-2 SAR Observations. *Geophys. Res. Lett.* **2020**, *47*, e2019GL086142. [CrossRef]

36. Zhao, C.; Kang, Y.; Zhang, Q.; Lu, Z.; Li, B. Landslide Identification and Monitoring along the Jinsha River Catchment (Wudongde Reservoir Area), China, Using the InSAR Method. *Remote Sens.* **2018**, *10*, 993. [CrossRef]

37. Liu, Q.; Liu, S.; Zhang, Y.; Wang, X.; Zhang, Y.; Guo, W.; Xu, J. Recent shrinkage and hydrological response of Hailuogou glacier, a monsoon temperate glacier on the east slope of Mount Gongga, China. *J. Glaciol.* **2010**, *56*, 215–224. [CrossRef]

38. Zheng, G.; Bao, A.; Allen, S.; Antonio Ballesteros-Cánovas, J.; Yuan, Y.; Jiapaer, G.; Stoffel, M. Numerous unreported glacial lake outburst floods in the Third Pole revealed by high-resolution satellite data and geomorphological evidence. *Sci. Bull.* **2021**, *66*, 1270–1273. [CrossRef]

39. Tan, J.; Huffman, G.J.; Bolvin, D.T.; Nelkin, E.J. IMERG V06: Changes to the Morphing Algorithm. *J. Atmos. Ocean. Technol.* **2019**, *36*, 2471–2482. [CrossRef]

40. Hersbach, H.; Bell, B.; Berrisford, P.; Hirahara, S.; Horanyi, A.; Munoz-Sabater, J.; Nicolas, J.; Peubey, C.; Radu, R.; Schepers, D.; et al. The ERA5 global reanalysis. *Q. J. R. Meteorol. Soc.* **2020**, *146*, 1999–2049. [CrossRef]

41. Li, D.; Shangguan, D.; Wang, X.; Ding, Y.; Su, P.; Liu, R.; Wang, M. Expansion and hazard risk assessment of glacial lake Jialong Co in the central Himalayas by using an unmanned surface vessel and remote sensing. *Sci. Total Environ.* **2021**, *784*, 147249. [CrossRef]

42. Song, C.; Huang, B.; Ke, L.; Richards, K.S. Remote sensing of alpine lake water environment changes on the Tibetan Plateau and surroundings: A review. *ISPRS J. Photogramm. Remote Sens.* **2014**, *92*, 26–37. [CrossRef]

43. Qiao, B.; Zhu, L.; Yang, R. Temporal-spatial differences in lake water storage changes and their links to climate change throughout the Tibetan Plateau. *Remote Sens. Environ.* **2019**, *222*, 232–243. [CrossRef]

44. Zhang, G.; Yao, T.; Xie, H.; Yang, K.; Zhu, L.; Shum, C.K.; Bolch, T.; Yi, S.; Allen, S.; Jiang, L.; et al. Response of Tibetan Plateau lakes to climate change: Trends, patterns, and mechanisms. *Earth Sci. Rev.* **2020**, *208*, 103269. [CrossRef]

45. Mandanici, E.; Bitelli, G. Preliminary Comparison of Sentinel-2 and Landsat 8 Imagery for a Combined Use. *Remote Sens.* **2016**, *8*, 1014. [CrossRef]

46. Yang, L.; Lu, Z.; Zhao, C.; Kim, J.; Yang, C.; Wang, B.; Liu, X.; Wang, Z. Analyzing the triggering factors of glacial lake outburst floods with SAR and optical images: A case study in Jinweng Co, Tibet, China. *Landslides* **2022**, *19*, 855–864. [CrossRef]

47. Strozzi, T.; Luckman, A.; Murray, T.; Wegmuller, U.; Werner, C.L. Glacier motion estimation using SAR offset-tracking procedures. *IEEE Trans. Geosci. Remote Sens.* **2002**, *40*, 2384–2391. [CrossRef]

48. Wegnüller, U.; Werner, C.; Strozzi, T.; Wiesmann, A.; Frey, O.; Santoro, M. Sentinel-1 Support in the GAMMA Software. *Procedia Comput. Sci.* **2016**, *100*, 1305–1312. [CrossRef]

49. Berardino, P.; Fornaro, G.; Lanari, R.; Sansosti, E. A new algorithm for surface deformation monitoring based on small baseline differential SAR interferograms. *IEEE Trans. Geosci. Remote Sens.* **2002**, *40*, 2375–2383. [CrossRef]

50. Li, S.; Xu, W.; Li, Z. Review of the SBAS InSAR Time-series algorithms, applications, and challenges. *Geod. Geodyn.* **2022**, *13*, 114–126. [CrossRef]

51. Goldstein, R.M.; Werner, C.L. Radar interferogram filtering for geophysical applications. *Geophys. Res. Lett.* **1998**, *25*, 4035–4038. [CrossRef]

52. Costantini, M. A novel phase unwrapping method based on network programming. *IEEE Trans. Geosci. Remote Sens.* **1998**, *36*, 813–821. [CrossRef]

53. Song, C.; Huang, B.; Richards, K.; Ke, L.; Hien Phan, V. Accelerated lake expansion on the Tibetan Plateau in the 2000s: Induced by glacial melting or other processes? *Water Resour. Res.* **2014**, *50*, 3170–3186. [CrossRef]

54. Holmes, J.A.; Cook, E.R.; Yang, B. Climate change over the past 2000 years in Western China. *Quat. Int.* **2009**, *194*, 91–107. [CrossRef]

55. Small, R.J. Lateral Moraines of Glacier De Tsidjiore Nouve: Form, Development, and Implications. *J. Glaciol.* **2017**, *29*, 250–259. [CrossRef]

56. Deline, P.; Gruber, S.; Delaloye, R.; Fischer, L.; Geertsema, M.; Giardino, M.; Hasler, A.; Kirkbride, M.; Krautblatter, M.; Magnin, F.; et al. Chapter 15—Ice Loss and Slope Stability in High-Mountain Regions. In *Snow and Ice-Related Hazards, Risks, and Disasters*; Shroder, J.F., Haeberli, W., Whiteman, C., Eds.; Academic Press: Boston, MA, USA, 2015; pp. 521–561. [CrossRef]

57. Gurung, D.R.; Khanal, N.R.; Bajracharya, S.R.; Tsering, K.; Joshi, S.; Tshering, P.; Chhetri, L.K.; Lotay, Y.; Penjor, T. Lemthang Tsho glacial Lake outburst flood (GLOF) in Bhutan: Cause and impact. *Geoenvironmental Disasters* **2017**, *4*, 17. [CrossRef]

58. Liu, G.; Zhang, B.; Zhang, R.; Cai, J.; Fu, Y.; Liu, Q.; Yu, B.; Li, Z. Monitoring Dynamics of Hailuogou Glacier and the Secondary Landslide Disasters Based on Combination of Satellite SAR and Ground-Based SAR. *Geomat. Inf. Sci. Wuhan Univ.* **2019**, *44*, 980–995. [CrossRef]

59. Pratap, B.; Sharma, P.; Patel, L.; Singh, A.T.; Gaddam, V.K.; Oulkar, S.; Thamban, M. Reconciling High Glacier Surface Melting in Summer with Air Temperature in the Semi-Arid Zone of Western Himalaya. *Water* **2019**, *11*, 1561. [CrossRef]

60. van Woerkom, T.; Steiner, J.F.; Kraaijenbrink, P.D.A.; Miles, E.S.; Immerzeel, W.W. Sediment supply from lateral moraines to a debris-covered glacier in the Himalaya. *Earth Surf. Dyn.* **2019**, *7*, 411–427. [CrossRef]

61. Guo, R.; Li, S.; Chen, Y.n.; Li, X.; Yuan, L. Identification and monitoring landslides in Longitudinal Range-Gorge Region with InSAR fusion integrated visibility analysis. *Landslides* **2020**, *18*, 551–568. [CrossRef]

62. Liu, X.; Wang, Y.; Koo, R.C.H.; Kwan, J.S.H. Development of a slope digital twin for predicting temporal variation of rainfall-induced slope instability using past slope performance records and monitoring data. *Eng. Geol.* **2022**, *308*, 106825. [CrossRef]

63. Kuang, X.; Jiao, J.J. Review on climate change on the Tibetan Plateau during the last half century. *J. Geophys. Res. Atmos.* **2016**, *121*, 3979–4007. [CrossRef]